

The First Automatic Method for Mapping the Pothole in Seagrass

Maryam Rahnemoonfar

Masoud Yari

School of Engineering and Computing Sciences

Texas A&M University-Corpus Christi

Maryam.Rahnemoonfar@tamucc.edu

Masoud.Yarir@tamucc.edu

Abdullah Rahman

Richard Kline

School of Earth, Environmental,

and Marine Sciences

University of Texas Rio Grande Valley

abdullah.rahman@utrgv.edu

richard.kline@utrgv.edu

Abstract

There is a vital need to map seagrass ecosystems in order to determine worldwide abundance and distribution. Currently there is no established method for mapping the pothole or scars in seagrass. Detection of seagrass with optical remote sensing is challenged by the fact that light is attenuated as it passes through the water column and reflects back from the benthos. Optical remote sensing of seagrass is only possible if the water is shallow and relatively clear. In reality, coastal waters are commonly turbid, and seagrasses can grow under 10 meters of water or even deeper. One of the most precise sensors to map the seagrass disturbance is side scan sonar. Underwater acoustics mapping produces a high definition, two-dimensional sonar image of seagrass ecosystems. This paper proposes a methodology which detects seagrass potholes in sonar images. Side scan sonar images usually contain speckle noise and uneven illumination across the image. Moreover, disturbance presents complex patterns where most segmentation techniques will fail. In this paper, the quality of image is improved in the first stage using adaptive thresholding and wavelet denoising techniques. In the next step, a novel level set technique is applied to identify the pothole patterns. Our method is robust to noise and uneven illumination. Moreover it can detect the complex pothole patterns. We tested our proposed approach on a collection of underwater sonar images taken from Laguna Madre in Texas. Experimental results in comparison with the ground-truth show the efficiency of the proposed method.

1. Introduction

Almost 65% of original seagrass communities have been lost over time in Europe, North America, and Australia because of indirect and direct effects of humans [7]. The widespread loss of seagrass beds is largely caused by the rapid expansion of human populations around coastal waterways[7]. The removal of seagrass for the creation of harbors and channels are examples of direct impact. Additionally, coastal expansion will result in an increase in recreational and commercial activities on the water.

A variety of remote sensing approaches have been used for mapping and observing seagrass since the 1990s [2]. Detection of seagrass with optical remote sensing (both satellite imagery and aerial photography) is complicated by the fact that light is attenuated as it passes through the water column and reflects back from the benthos. Attenuation is a function of the overlying water column's depth and sediment loads. Therefore, optical remote sensing of seagrass is only possible if the water is shallow and relatively clear. In reality, coastal waters are commonly turbid, and seagrasses can grow under 10 meters of water or even deeper. The principal advantage of optical remote sensing in identifying, classifying and mapping of terrestrial vegetation is the high contrast between the visible and the near-infrared (NIR) reflectance of vegetation, which has led to the development of Vegetation Index (VI) for quantifying vegetation greenness and health. However this approach is not feasible for remote sensing of seagrass, because the overlying water column absorbs the NIR spectrum of light. Only the visible bands of multispectral satellite sensors, (e.g., Landsat) are commonly used to map seagrass habitats in coastal waters [8]. Water absorption of NIR limits the utility of optical remote

sensing for mapping seagrass health or disturbance. Additionally, pixels sizes of the freely available satellite images vary from 30 m (Landsat) to 250 m (MODIS), which are not adequate for mapping the propeller scars or other disturbances that occur at much smaller spatial scales. Spectral mixture analysis (SMA) has recently been applied to quantify the percentage of vegetated and disturbed areas within a satellite pixel [1], but with little success. Additionally, SMA cannot produce a detailed map of the disturbed areas.

Underwater acoustics mapping produces a high definition, two-dimensional sonar image of seagrass ecosystems. The acoustic profile of this benthic ecosystem is created when sound waves are relayed from the transducer of a sonar device. The intensity and contours of the image are then determined by the amount of time a sound wave takes to return to the transducer and how the waves were reflected.

1.1. Related work

Pattern recognition techniques have been applied on sonar images for detecting concrete objects mainly on sandy sea floor. A Markovian segmentation algorithm was used by Mignotte et al. [10] to segment the sonar image. Additionally, Mignotte et al. created another method[11] where they segmented sonar images using an unsupervised hierarchical MRF model to segment shadow and sea-bottom reverberation. Even though they obtained good results for simple objects on sandy sea floor, their particular method would be complicated and computationally costly to segment seagrass images with complex patterns. Furthermore, another sonar segmentation method is described by Lianantonakis et al. [6]. Their particular research focuses on the segmenting of sonar images. The first step on their method is to extract texture features from a sonar image which contains only two regions. Then, an active contour model is applied on the feature image. An automatic approach for the detection of meter-sized concrete artificial reefs on the sea floor was proposed by Tian et al. [12]. In this algorithm features were extracted using co-occurrence matrix and then classified by a Bayesian classifier. Another sonar image segmentation method was created by Ye et al. [13]. Based on Gauss-Markov random field model and the level-set energy functions, they first extracted the local features of sonar images. Although the side scan sonar (SSS) has been used for benthic mapping there is no existing method that automatically detects the extent of seagrass beds or automatically identifies and maps its disturbance.

Sonar images usually suffer from having speckle noise which makes it difficult to segment continuous seagrass areas vs. disturbances. Additionally, brightness levels throughout the entire image can be non-uniform, which make a real challenge in the segmentation of natural and man-made disturbance in sea-grass. Moreover, disturbance presents complex patterns where most segmentation tech-

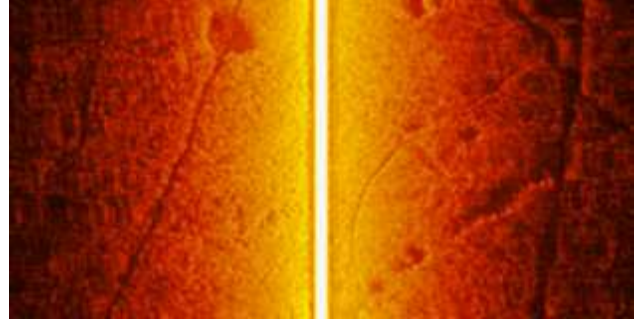


Figure 1. Sidescan sonar image with uneven illumination across the image.

niques would normally fail. Here we propose a novel technique that will address all of the issues in a three-step procedure.

In this paper, we propose a three-phase model for recognition of potholes on seagrass structure depicted on sonar images. In the first step, adaptive thresholding will be applied on the sonar images to uniform the brightness value; in the second step, wavelet transformation will be applied on the image to reduce the speckle noise. Finally a novel level set algorithm is developed to detected natural and man-made disturbance in seagrass.

1.2. Sensing modality

Side scan sonar uses two parallel transducers to transfer a high frequency acoustic signal in the water. The transducers are installed underneath a ‘towfish,’ which stays suspended in water and is dragged by a boat traveling at an optimum speed of five to six knots. The acoustic signal is sent out at a narrow beam angle perpendicular to the boat’s direction. The signal travels to the sea floor, and the strength of the reflected signal depends on the morphology and nature of the sea bottom. Reflected signal is received by the transducers and transmitted to a recorder on the boat. The elapsed time between the emitted and the reflected signals gives the location of an object. Side-scan sonar images often show striking variations in brightness due to the fact that objects closer to the transducer will create higher reflections. Figure 1 shows a sonar image. As it can be seen in Figure 1 the brightness values varies across the image. In the middle of the image, where the boat is moving there is higher intensity of reflection and the image is bright while in the side of the image, the reflection is of lower intensity and the image looks darker.

2. Proposed approach

Sonar images suffer from speckle noise and uneven illumination. Seagrass disturbance present complex patterns. It is much harder to detect seagrass disturbance patterns and

potholes than detecting concrete objects with regular geometric shape. We address these challenges in three phases. To compensate the uneven illumination in reflectance, we use adaptive thresholding. To remove noise we use wavelet transform and finally to detect pothole we use a novel level set technique.

2.1. Adaptive thresholding

To compensate the non-uniformities in reflectance we used Gaussian adaptive thresholding technique. In this method, a variable threshold was calculated at every point, (x,y) based on the properties computed in a neighborhood of (x,y). In Gaussian adaptive thresholding, the threshold value is a weighted sum of the small neighborhood around pixel. The neighborhood windows are chosen small enough so that the illumination of each is approximately uniform. A threshold is calculated for each pixel based on the convolution of the image with Gaussian function as following:

$$T(x, y) = \sum_{k=-a}^a \sum_{l=-b}^b G(s, t) f(x - k, y - l) \quad (1)$$

where G is the Gaussian function of two variables and has the basic form of

$$G(x, y) = \frac{1}{2\pi\sigma^2} e^{-\frac{x^2+y^2}{2\sigma^2}} \quad (2)$$

where σ is the standard deviation.

2.2. Wavelet Denoising

Image acquisition by sonar sensor produces some speckle noise and it is necessary to remove them before further processing. There are generally two ways to remove noise from the image: 1- Spatial domain, 2- transformed domain. In the first approach, the noise reduction operators will be carried on the grey values of the original image such as mean, median, and adaptive filters. However, in the second approach the procedure will be performed on the transformed images. The wavelet denoising belongs to the second category.

Given the noisy image $g(x, y)$, the objective is to get an estimation of the original image, using the wavelet denoising technique (Equation 3).

$$g(x, y) = f(x, y) + \eta(x, y) \quad (3)$$

At each step of the wavelet transform, the image is decomposed into four quarter-size image. Each of the four images is formed by convolution with one of the wavelet basis function, followed by subsampling in x and y by a factor of two. Since the scaling and wavelet functions are separable, each convolution can be broken down to one-dimensional convolutions on the rows and columns. In this way, at the

stage one, we convolve the rows of the image with low pass and high pass filters g and h and downsample the columns. The columns then will be convolved with low pass and high pass filters and the rows will be downsampled [9]. The result is the four $N/2$ -by $N/2$ arrays required for this stage of the transform (Figure 2).

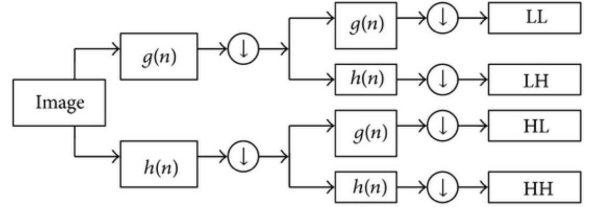


Figure 2. Two dimensional discrete wavelet transform (DWT)

The basic procedure for our wavelet denoising is as follows:

1. padding the width and height of the dimensions of the image to make sure that the dimensions are a power of two;
2. calculate the DWT of the image. Here we applied the 2D Haar wavelet transform;
3. shrinking the coefficients by using the soft thresholding;
4. compute the IDWT to get the denoised estimate;
5. remove the padding to get the regular image without the noise.

2.3. Pattern identification using levelset

Due to a large complexity of patterns in natural and manmade seagrass disturbance, ordinary pattern recognition techniques fail to segment seagrass from disturbance. Here we propose to use the level set technique to extract and map disturbance in seagrass. The level set method (LSM) is essentially a successor to the active counter method. Active contour method (ACM), also known as Snake Model, was first introduced in the context of image processing [3] . The ACM is designed to detect interfaces and boundaries, of an object in image for instance, by a set of parametrized curves (contours) that march successively toward the desired object until the desired interface is captured. The ACM is an efficient tool in image and video segmentation, but it suffers from certain serious issues, such as the need to handle changes in topology of the active contour explicitly. The LSM method overcomes this issue by capturing the boundaries of desired objects in the image as the intersection of

a higher dimensional surface, called the Level Set Function (LSF), with the zero-level plane.

In the context of image segmentation and object detection, the LSF is the solution of an initial boundary value problem. Let $\varphi = \varphi(x, t)$ present the LSF, where t is the time, and x is the spatial variable defined on an image region, which we denote by Ω . The equation reads

$$\begin{aligned} \frac{\partial \varphi}{\partial t} &= \mathcal{E}(\varphi), & t > 0, x \in \Omega; \\ \varphi(x, 0) &= \varphi_0, & x \in \Omega. \end{aligned} \quad (4)$$

Here \mathcal{E} is the energy functional whose form will be dictated by the specific application. In most cases of object detection problems, fundamental features that contribute to the energy functional are the edge and the area; therefore,

$$\mathcal{E} = E(\varphi) + A(\varphi) \quad (5)$$

In this formulation, the first term presents the edge functional, and the second term is the area term. We define them as follows

$$E(\varphi) = \lambda \int_{\Omega} g \delta(\varphi) |\nabla \varphi| dx \quad (6)$$

$$A(\varphi) = \alpha \int_{\Omega} g H(-\varphi) dx \quad (7)$$

where α is a real constant and $\lambda > 0$; the function g is an edge indication function; δ and H are the Dirac and Heaviside functions respectively. We will approximate them by

$$\delta_{\varepsilon}(x) = \begin{cases} \frac{1}{2\varepsilon} (1 + \cos(\frac{\pi x}{\varepsilon})) & |x| \leq \varepsilon, \\ 0 & |x| > \varepsilon; \end{cases} \quad (8)$$

and

$$H_{\varepsilon}(x) = \begin{cases} \frac{1}{2} (1 + \frac{x}{\varepsilon} + \frac{1}{\pi} \sin(\frac{\pi x}{\varepsilon})) & |x| \leq \varepsilon, \\ 1 & x > \varepsilon, \\ 0 & x < -\varepsilon; \end{cases} \quad (9)$$

where $\varepsilon > 0$ is a small constant.

To solve Equation 4, we will assume $|\nabla \varphi| = 1$. This assumption will pose a computational difficulty. In the conventional formulation of the LSM, the unit vector size assumption for $|\nabla \varphi|$ will not be necessarily kept through iteration steps. This can introduce irregularities in the computational process. To avoid it, a need for re-initialization at each time step may be necessary. However, this will result in a high computational cost. Several approaches have been suggested to avoid the high computational cost. We believe one of the best approaches to for overcoming the issue of irregularities and re-initialization is suggested in [4]

and completed in [5]. Inspired by certain phenomena in fluid dynamics, we will add a diffusion type functional to stabilize the process without need of re-initialization. The new formulation of the energy functional reads

$$\mathcal{E} = E(\varphi) + A(\varphi) + \text{div}(D \nabla \varphi) \quad (10)$$

where the last term is called the distance regularization term, with a diffusion coefficient $D = D(\varphi)$. This diffusion coefficient is constructed from a double-well potential function p . We will define

$$D(\varphi) = \frac{p'(|\nabla \varphi|)}{|\nabla \varphi|} \quad (11)$$

where

$$p(s) = \begin{cases} (1 - \cos(2\pi s))/4\pi^2 & s \leq 1; \\ (s - 1)^2/2 & s \geq 1. \end{cases} \quad (12)$$

Given the above formulation, one can drive the energy minimization PDE system:

$$\begin{aligned} \frac{\partial \varphi}{\partial t} &= \lambda \delta_{\varepsilon}(\varphi) \text{div} \left(g \frac{\nabla \varphi}{|\nabla \varphi|} \right) \\ &\quad + \alpha g \delta_{\varepsilon}(\varphi) \\ &\quad + \mu \text{div} \left(\frac{p'(|\nabla \varphi|)}{|\nabla \varphi|} \nabla \varphi \right) & t > 0, x \in \Omega; \end{aligned} \quad (13)$$

$$\varphi(x, 0) = \varphi_0(x), \quad x \in \Omega;$$

$$\nabla \cdot \varphi = 0, \quad \text{on } \partial \Omega.$$

The last equation expresses the Neumann boundary condition. The initial condition is set by the middle equation. The initialization function is commonly considered to be a step function defined as

$$\varphi_0 = \begin{cases} -c_0 & x \in \Omega_0, \\ c_0 & x \in \Omega/\Omega_0; \end{cases} \quad (14)$$

where $c_0 > 0$ is a constant, and Ω_0 is a region inside the image region Ω .

In most applications of the LSM, the object to be captured has some sort of regularity; or there are other features in the image that can contribute to the convergence of the LS process. Our images are highly noisy; moreover, there is a track left by the boat in each image. However, our experiments show that the choice of an initial region Ω_0 is flexible as long as it is not too big or wide. We will treat the desired object as a self-organized entity. In this way, the object will be captured gradually starting from a simple pattern that will grow to a more complex one. The presence of the diffusion term in the Equation 13 prevents the destabilizing effects of other terms.

One final tuning in the algorithm will be the addition of the narrow band technique. As described at the beginning of this section, the LSM will take our two dimensional problem to a three dimensional level. This is going to respect the topology of initialization function through the process, unlike the ACM. However, this comes with a higher computational price: instead of two-dimensional object, we will be capturing a three-dimensional one. Therefore, to boost up our computation we will also implement a LS technique known as the narrow band technique. In this approach, our computation is performed in a narrow neighborhood of the level set curve in the level set function. In other words, instead of updating the entire level set function in each time step, we will update only a small neighborhood of the level set curve on the surface of the level set function.

3. Results

3.1. Data collection

The data was collected in Laguna Madre which contains 75% of the seagrass of Texas’s coastline.

To collect data we built a prototype side scan sonar (Figure 3).



Figure 3. Our prototype side scan sonar.

We used two Lowrance Structure Scan HD LSS-2 transducers as our side scan transducers. These transducers can produce 455 KHz and 800 KHz frequencies. Our bathymetric sounder is a Dual Beam 200 KHz transducer. All three of these transducers were connected to a Huminbird 998c HD SI combo head unit. We built a towfish from a 1.2 m long, 7.5 cm diameter, galvanized steel pipe, capped one end and attached four fins at the other end to stabilize and streamline its movement under water. The transducers were

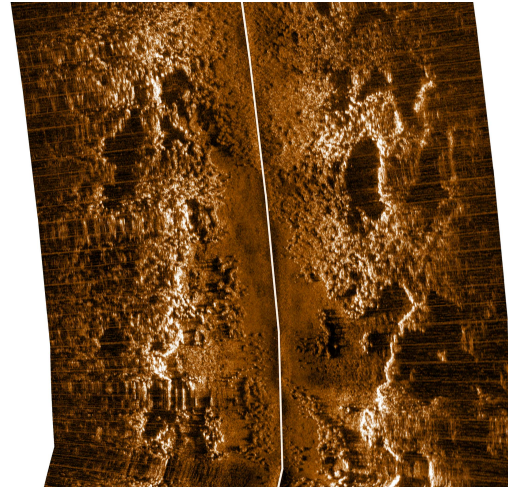


Figure 4. The sonar image collected with our prototype sonar.

installed on the bottom of the towfish. The towfish was immersed in water using a crane in front of a 21-ft boat. The boat was driven at a constant speed of six knots. Each reflected beam produces one narrow line of sonogram of the sea floor from both sides of the boat, at a pixel size depending on the sonar frequency, intensity, and ‘ping’ rate of the transducer. Boat’s position is measured with a GPS receiver, and the water’s depth is determined using a bathymetric sounder. Navigation information is recorded continuously along with the reflected acoustic signals. Combining each line of reflected signal with its position, time and depth, and mosaicking all lines in the chronological sequence produces an image of the seafloor (Figure 4). A mosaic of size approximately 5000×60000 pixels covering an area of about $12,000 m^2$ was created in this research.

3.2. Experimental results

The proposed method was tested on several sonar images collected from Laguna Madre. Figure 4 shows a representative image.

As it can be seen in Figure 4, the image has different illumination across the image. The image is brighter in the center, while towards the edge the image gets darker. In addition, all of sonar images have speckle noise. Here we applied adaptive thresholding and wavelet denoising to attenuate noise and improve uneven illumination (Figure 5).

After this step the proposed level set technique was applied on the sonar image to detect pothole patterns in seagrass. Figure 6 shows the result of the proposed method applied on Figure 5. In Figure 6, the top picture shows the initial curve for level set method, the middle image shows the result of the method after 250 iterations, and the last image shows the result of the method after 750 iterations. As it



Figure 5. The sonar image after removing uneven illumination and noise using adaptive thresholding and wavelet denoising.

can be seen, although the initial curve is located only on the center of the image, after 250 iterations, it will evolve and detect almost all potholes in the sonar image. By increasing the iterations number, some of the curves will be merged together, some of the curves will grow and some of them will split. Finally after 750 iterations the results converge.

In the next test (Figure 7), both open curve and closed curves are depicted as the initial curve. Figure 7 shows the disturbance pattern of seagrass with this initial curve and in different iterations. Here the level set converges with lower number of iterations. Some part of the boat path is separated from pothole.

3.3. Evaluation

To evaluate the performance of our proposed method first we need to set up some benchmarks. For any particular piece of data that we are evaluating there are four states. Whether it correctly belongs to a class or does not belong to a class. This information is normally displayed in a confusion matrix. In confusion matrix, TP is true positive or correct result, FP is false positive or unexpected result, FN is false negative or missing results, and TN is true negative. From the confusion matrix recall (R) and precision (P) are calculated as follow:

$$P = \frac{TP}{TP + FP} \quad (15)$$

Precision, the exactness of a classifier, and recall, the completeness of a classifier, can be combined to produce a single metric known as *F-measure*, which is the weighted harmonic mean of precision and recall. The F-measure, defined in Equation 16, captures the precision and recall trade-off.

$$F = \frac{1}{\frac{\alpha}{P} + \frac{1-\alpha}{R}} = \frac{(\beta^2 + 1)PR}{\beta^2 P + R}, \quad (16)$$

The F-measure varies between 0 and 1, where larger values are more wanted. In this paper we used balanced F-

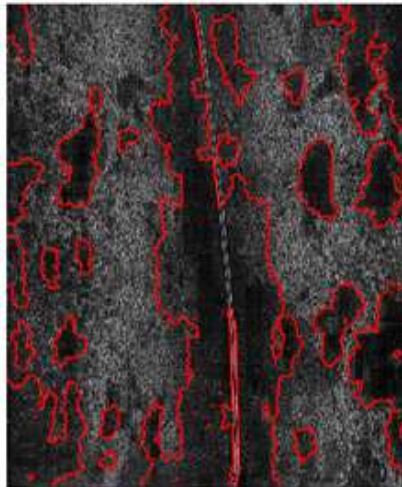
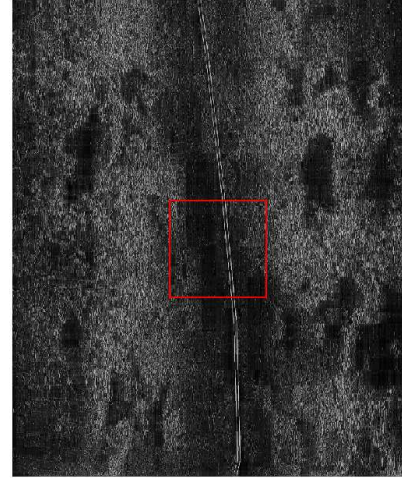


Figure 6. Disturbance pattern depicted by the propose method. Top:Initial curve middle: disturbance pattern after 250 iterations Bottom: disturbance pattern after 750 iterations

measure, i.e. with $\beta = 1$.

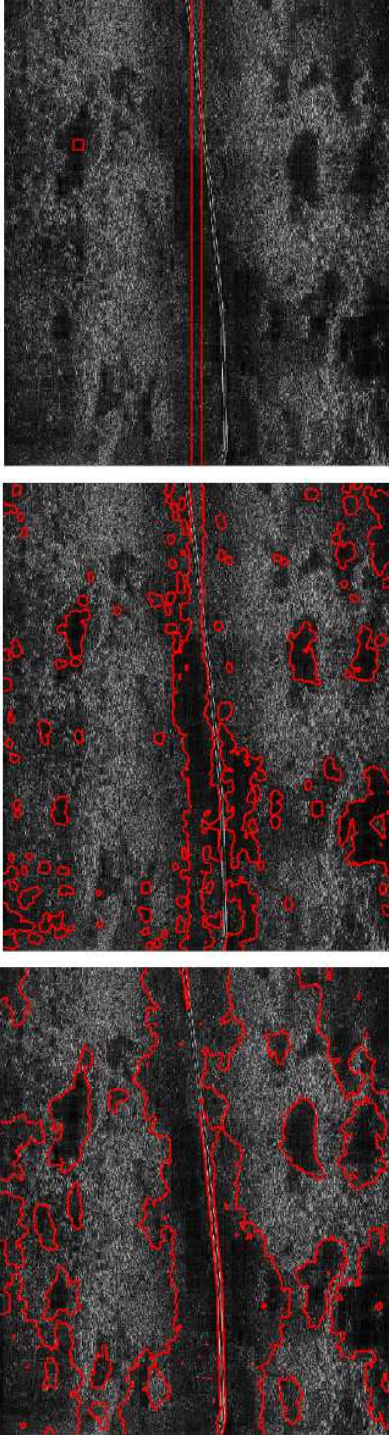


Figure 7. Disturbance pattern depicted by the propose method. Top: Initial curve middle: disturbance pattern after 250 iterations Bottom: disturbance pattern after 500 iterations

After setting up our benchmarks, we calculated the F-measure of each output with respect to the ground-truth. Figure 9 shows the representative ground-truth result. Here

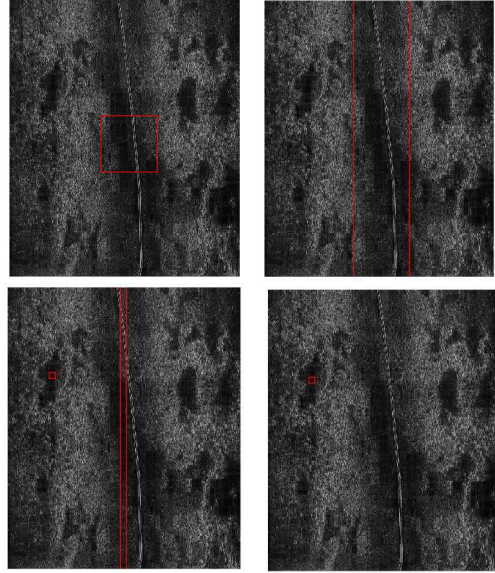


Figure 8. The initial curve for different experiments.

the expert manually labeled the boundary of pothole in sonar image. We calculated precision, recall and F-measure for all images in dataset in respect to the ground-truth image. Table 1 shows the average precision, recall, and F-measure in our experiment.

Precision	Recall	F-Measure
0.83	0.73	0.78

Table 1. Evaluation of our results.

We tested our algorithm with different initial curves.

Figure 8 shows the initial curves of different experiments. Our experiment shows that the location of initial curve does not have great effect on final accuracy (Table 2 and 3). A random initial curve on any part of the image will automatically detect all of the boundaries. However, the more accurate initial curve on areas where potholes are located will result in a faster convergent of the evolving curve. For example, because the closed initial curve in Figure 7 contains only the pothole, the proposed approach could converge with higher speed.

4. Conclusion

In this paper, we proposed an automatic approach which detects seagrass potholes in sonar images. In the first step we used the adaptive thresholding and wavelet denoising to remove the uneven illumination and noise that are available in sonar images. In next step we proposed an automatic levelset technique which detects the boundary of pothole quickly. The proposed method was applied on sonar images

	TP	TN	FP	FN
Exp1	277814	296326	57462	102985
Exp2	289818	276093	74069	90981
Exp3	271768	305026	48593	109031
Exp4	271113	300933	53869	109686

Table 2. Confusion matrix for different experiments in Figure 8.

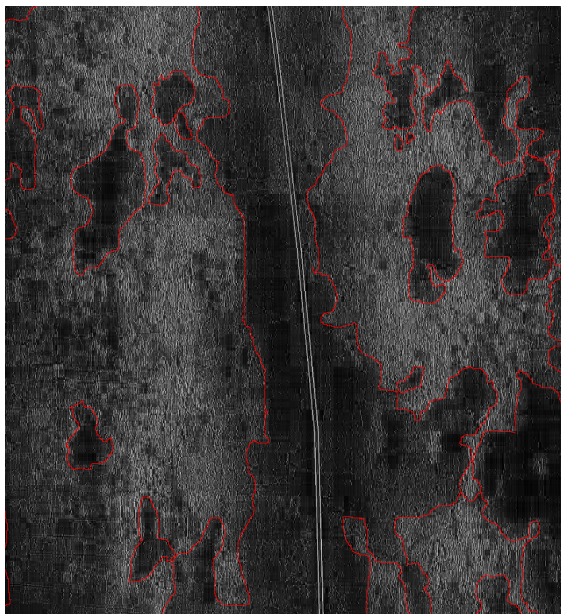


Figure 9. Ground-truth result.

	Precision	Recall	F-Measure
Exp1	0.83	0.73	0.78
Exp2	0.80	0.76	0.78
Exp3	0.85	0.71	0.78
Exp4	0.83	0.71	0.77

Table 3. Evaluation of our results for experiments with various initial curve location.

taken from Laguna Madre in Texas. Experimental results in comparison with the ground truth show the high accuracy of the proposed technique. In future we are planning to extend this work for real-time identification of seagrass disturbance patterns.

References

[1] A. Bargain, M. Robin, E. Le Men, A. Huete, and L. Barillé. Spectral response of the seagrass *zostera noltii* with different sediment backgrounds. *Aquatic Botany*, 98(1):45–56, 2012.

[2] M. S. Hossain, J. S. Bujang, M. Zakaria, and M. Hashim. Assessment of landsat 7 scan line corrector-off data gap-filling methods for seagrass distribution mapping. *International Journal of Remote Sensing*, 36(4):1188–1215, 2015.

[3] M. Kass, A. Witkin, and D. Terzopoulos. Snakes: Active contour models. *International journal of computer vision*, 1(4):321–331, 1988.

[4] C. Li, C. Xu, C. Gui, and M. D. Fox. Level set evolution without re-initialization: a new variational formulation. In *Computer Vision and Pattern Recognition, 2005. CVPR 2005. IEEE Computer Society Conference on*, volume 1, pages 430–436. IEEE, 2005.

[5] C. Li, C. Xu, C. Gui, and M. D. Fox. Distance regularized level set evolution and its application to image segmentation. *IEEE Transactions on image processing*, 19(12):3243–3254, 2010.

[6] M. Lianantonakis and Y. R. Petillot. Sidescan sonar segmentation using active contours and level set methods. In *Oceans 2005-Europe*, volume 1, pages 719–724. IEEE, 2005.

[7] H. K. Lotze, H. S. Lenihan, B. J. Bourque, R. H. Bradbury, R. G. Cooke, M. C. Kay, S. M. Kidwell, M. X. Kirby, C. H. Peterson, and J. B. Jackson. Depletion, degradation, and recovery potential of estuaries and coastal seas. *Science*, 312(5781):1806–1809, 2006.

[8] M. B. Lyons, S. R. Phinn, and C. M. Roelfsema. Long term land cover and seagrass mapping using landsat and object-based image analysis from 1972 to 2010 in the coastal environment of south east queensland, australia. *ISPRS Journal of Photogrammetry and Remote Sensing*, 71:34–46, 2012.

[9] Y. Meyer. *Wavelets and operators*, volume 1. Cambridge university press, 1995.

[10] M. Mignotte, C. Collet, P. Pérez, and P. Bouthemy. Three-class markovian segmentation of high-resolution sonar images. *Computer Vision and Image Understanding*, 76(3):191–204, 1999.

[11] M. Mignotte, C. Collet, P. Perez, and P. Bouthemy. Sonar image segmentation using an unsupervised hierarchical mrf model. *IEEE transactions on image processing*, 9(7):1216–1231, 2000.

[12] W.-M. Tian. Automatic target detection and analyses in sidescan sonar imagery. In *Intelligent Systems, 2009. GCIS'09. WRI Global Congress on*, volume 4, pages 397–403. IEEE, 2009.

[13] X.-F. Ye, Z.-H. Zhang, P. X. Liu, and H.-L. Guan. Sonar image segmentation based on gmrf and level-set models. *Ocean Engineering*, 37(10):891–901, 2010.